

Laser ablation of Cu and plume expansion into 1 atm ambient gas

Zhaoyang Chen^{a)} and Annemie Bogaerts

Department of Chemistry, University of Antwerp, Universiteitsplein 1, B-2610 Wilrijk-Antwerp, Belgium

(Received 30 July 2004; accepted 11 January 2005; published online 14 March 2005)

A one-dimensional gas-dynamic model is presented for the laser ablation of Cu and the expansion of the Cu vapor in a background gas (He) at 1 atm. The ionization of Cu and He, the inverse bremsstrahlung absorption processes and photoionization process, and the back flux onto the target are considered simultaneously. The binary diffusion, the viscosity, and the thermal conduction including the electron thermal conduction are considered as well. Numerical results show that the consideration of ionization and laser absorption in the plume greatly influences the gas dynamics. The ionization of Cu enables the recondensation at the target surface to happen even during the laser pulse. The ionization degree of Cu and He may change greatly with the location in the plume. For laser irradiances ranging from 2 to 9×10^{12} W/m², the simulations show that the second-order ionization of Cu competes with the first-order ionization. In the region close to the target surface, the first-order ionization of Cu dominates. In the core of the plasma, the second-order ionization of Cu may dominate over the first-order ionization at laser irradiances higher than 7×10^{12} W/m². In the mixing layer, the first-order ionization of Cu is always more important than the second-order ionization although the latter increases monotonously with laser irradiance. The ionization of He is only important in the mixing layer. The plume expansion velocity is much larger than that without ionization and laser absorption by the plume. The relative importance of different laser absorption mechanisms may change with time. Close to the surface photoionization and electron-neutral inverse bremsstrahlung are always important. Once the ionization in the plume starts, at later time, electron-ion inverse bremsstrahlung can become more important than photoionization in the plume core until the shock wave front. Unlike in the vacuum case, electron-neutral inverse bremsstrahlung is very strong due to the relatively high number density of neutral atoms in the plume in the presence of a dense ambient gas. A similar laser irradiance threshold is found for the ablation rate and the plasma formation in the plume, which agrees well with the case of nanosecond laser ablation of metals in vacuum. © 2005 American Institute of Physics. [DOI: 10.1063/1.1863419]

I. INTRODUCTION

Laser ablation (LA) is used for a growing number of applications, such as pulsed laser deposition (PLD),^{1,2} nanoparticle manufacturing,^{3,4} cluster production,⁵ for the analysis of solid materials,⁶⁻⁹ etc. The study of material expanding into vacuum or in ambient background gas is an important issue in gas dynamics (see Ref. 10) and for laser ablation. Laser pulses used in PLD have typically a duration of several tens of nanoseconds and an energy fluence of several J/cm². The quality of the deposited film depends critically on the range and profile of the kinetic energy of the ablated plume. To reduce the plume kinetic energy, the technique of PLD in a buffer gas is used. In addition, the technique of PLD in a buffer gas also allows one to vary the film stoichiometry. Hence, it is of great importance to know the dynamics of a plume of ablated material in a background gas in order to optimize the experimental parameters during the film production process. However, when LA is used for solid material analysis, e.g., laser-induced breakdown spectroscopy (LIBS),¹¹ or LA as a sample introduction method for an inductively coupled plasma (ICP), the laser pulses have typically a laser irradiance between 10^8 and 10^9 W/cm² and a

duration of a few tens of nanoseconds, and for these applications the background gas is typically at 1 atm.⁶⁻⁹

The plume expansion can be investigated either by Monte Carlo (MC) simulations,¹²⁻¹⁶ by hydrodynamic models,^{3,17-25} or by a hybrid model (combination of both).^{26,27} Among the hydrodynamic models the pressure is mostly limited till maximum about 100 Pa.^{18,21-24} The plume expansion into 1-atm background gas was investigated only in Refs. 3, 17, 19, and 25. It should be mentioned that it would take much longer calculation time to study the plume expansion into a high-pressure background gas with the MC simulations or hybrid models. Therefore, generally one makes use of hydrodynamic models to study the plume expansion into 1-atm background gas. The general effect of the background gas is reported to be the spatial confinement and slowing down of the expanding plume. Moreover, the material can even move backward.^{3,28} Detalle *et al.* have experimentally studied the influence of long wavelengths on LIBS measurements under air or helium atmosphere.¹¹

Gnedovets *et al.*³ have reported a hydrodynamic model with two distinct species (material plume and background gas) and interactions between them. This model is applied to expansion in a background gas at 1 atm, but for a long laser pulse (millisecond-range) at very low laser irradiance (10^4 – 10^5 W/cm²), so that no plasma is formed. Very re-

^{a)}Author to whom correspondence should be addressed; electronic mail: zhaoyang.chen@ua.ac.be

cently, Gusarov and Smurov reported the expansion into 1-atm background gas for a short laser pulse (nanosecond-range) at higher laser irradiance (about 10^9 W/cm²),²⁵ but without taking into account the formation of plasma. However, at this high laser irradiance, the ionization of vapor and/or the background gas may become important and should be taken into account in the modeling.

There exist no models yet that describe the ionization of vapor and/or background gas for laser evaporation in 1-atm ambient gas. Such a modeling is, however, very important for the various applications mentioned above, where the laser irradiance is around 10^8 – 10^9 W/cm², and where evaporation takes place in 1-atm nonreactive background gas. The ionization of vapor during the laser ablation in vacuum has been studied (see, e.g., Refs. 29 and 30). In the present paper, we will extend and combine the methods explained in Refs. 25, 29, and 30 to describe the laser ablation of Cu and expansion into 1-atm ambient gas (He), including the ionization of both Cu and He. It is well known that, compared to the expansion into vacuum, the interaction of the plume with an ambient gas is a far more complex gas-dynamic process due to the occurrence of several physical processes involved, such as deceleration, attenuation, thermalization of the ablated species, diffusion, recombination, and formation of shock waves.³¹ Here we present a one-dimensional (1D) model for the laser interaction with a copper target, yielding heating, melting, and vaporization of the target material, followed by plume expansion into 1-atm He background gas, as well as plasma formation and shielding of the laser irradiance. Basically, the model is applied to nanosecond UV excimer or visible laser pulses, metal targets such as Cu or Al, and nonreactive ambient gas such as He or Ar. If there is a chemical reaction between the target element and the ambient gas, the model will fail. The irradiance ranges from 10^8 to 10^9 W/cm², which is typically used for laser ablation as a sample introduction method for ICP spectrometry. It can, however, also be of interest to other applications, which work under similar conditions.

It should be pointed out that the planar expansion of the plume in the early stage (e.g., till 100 ns which is derived from r_0/v_m , where the laser spot radius r_0 is about 1 mm and the maximum shock wave velocity is about 10^4 m/s) is justified. However, at later stages of the plume expansion, the plume may exhibit radial expansion too. Besides, at the later stages of the plume or plasma expansion, the assumption of local thermodynamic equilibrium is no longer valid because three-body recombination comes into play, which means that the Saha equation is not valid anymore. To study the later stages of plume expansion, the present model should be improved to include the detailed description of ionization and recombination mechanisms and the expansion along the radial direction. Hence, in the present paper, we only present results up till 100 ns.

II. MATHEMATICAL MODEL

The model presented in this paper describes several mechanisms, related to the laser-solid interaction and the behavior of the evaporated material and the background gas.

The different parts of the model will be described in detail below, and the coupling between the various parts will be discussed.

A. Target heating, melting, and vaporization

A large number of models for laser-solid interaction are based on thermal processes: heating of the solid, followed by melting, and evaporation. They describe the laser-solid interaction on a macroscopic scale, i.e., by the thermal heat conduction equation (e.g., Refs. 32–34 and the references therein). This assumption is justified for nanosecond-pulsed laser interaction, especially for metals. The theoretical description of laser-induced target heating and material removal was based on the model proposed in Ref. 34. The time-dependent temperature distribution along the target depth $T(t, z)$ is governed by the heat conduction equation in a one-dimensional form, as appropriate to many experimental situations,

$$c_p \rho \left[\frac{\partial T(t, z)}{\partial t} - u(t) \frac{\partial T(t, z)}{\partial z} \right] = \frac{\partial}{\partial z} \lambda \frac{\partial T(t, z)}{\partial z} + (1 - R_f) \alpha I(t) \exp(-\alpha z). \quad (1)$$

Here ρ is the mass density of the target material, c_p , λ , and α are the heat capacity, the thermal conductivity, and the absorption coefficient of the target. $I(t)$ is the laser irradiance at $z=0$. $u(t)$ is the velocity of surface recession and R_f is the reflection coefficient of the target surface. The latter is generally close to 1 for metals, but it can drop to values as low as 0.1 during laser ablation, when the laser irradiance is high enough. This is attributed to roughening due to the increase of the surface temperature, to removal of surface films, and to melting. In our model, we use a constant value of 0.34,³⁰ as indicated in Table I in order not to further complicate the solution of the heat conduction equation.

When the temperature at a certain depth in the target exceeds the melting point of Cu, the target starts melting, and the local temperature remains constant during the time that phase transition takes place. Further heating of the molten target is calculated in the same way, but using the data for molten Cu. Melting normally starts at the surface, but the melt front (i.e., the interface between solid and molten phase) can extend inside the target when the temperature rises further. The heat conduction equation is solved as a function of time during and after the laser pulse, with an explicit finite difference method.

When the temperature at the surface becomes very high, vaporization becomes significant. The saturation pressure P_s is calculated from the surface temperature, by integrating the Clausius–Clapeyron equation,³⁷

$$P_s(T_s) = p_0 \exp \left[\frac{\Delta H_{lv}(T_s - T_b)}{RT_s T_b} \right], \quad (2)$$

where T_s and T_b are the surface temperature and the normal boiling point at pressure $p_0=1$ atm, ΔH_{lv} is the heat of vaporization, and R is the gas constant. The data for a Cu target

TABLE I. Input data used in our model for Cu as a target material.

| Parameters | Values for Cu | Ref. |
|--|-----------------------------|----------|
| Thermal conductivity, λ (W m ⁻¹ K ⁻¹) | 380 (solid), 170 (liquid) | 29 |
| Specific heat, C_p (J kg ⁻¹ K ⁻¹) | 420 (solid), 494 (liquid) | 29 |
| Mass density, ρ (kg m ⁻³) | 8960 (solid), 8000 (liquid) | 1 and 29 |
| Absorption coefficient, α (m ⁻¹) | 7.44×10^7 | 29 |
| Reflectivity used in the model, R_f | 0.34 | 35 |
| Melting point, T_m (K) | 1358 | 1 |
| Boiling point, T_b (K) | 2836 | 1 |
| Heat of fusion, ΔH_{sl} (J/mol) | 1.3×10^4 | 1 |
| Heat of vaporization, ΔH_{lv} (J/mol) | 3.048×10^5 | 1 |
| First ionization potential, IP_1 (eV) | 7.73 | 36 |
| Second ionization potential, IP_2 (eV) | 20.29 | 36 |

are also presented in Table I, as well as the references where the data are taken from.

B. Expansion dynamics

The equations of continuity, vapor transport, momentum, and energy for a binary mixture are as follows:³⁸

$$\frac{\partial \rho}{\partial t} = -\frac{\partial \rho v}{\partial x}, \quad (3)$$

$$\frac{\partial \rho_v}{\partial t} = -\frac{\partial \rho_v v}{\partial x} + \frac{\partial}{\partial x} \left(\rho D_{ab} \frac{\partial \omega_v}{\partial x} \right), \quad (4)$$

$$\frac{\partial \rho v}{\partial t} = -\frac{\partial}{\partial x} \left(\rho v^2 + P + \frac{\partial}{\partial x} \tau_{xx} \right), \quad (5)$$

$$\begin{aligned} \frac{\partial}{\partial t} \left[\rho \left(U + \frac{1}{2} v^2 \right) \right] = & -\frac{\partial}{\partial x} \left[\rho \left(U + \frac{1}{2} v^2 \right) v + P v \right] \\ & - \frac{\partial}{\partial x} (q + v \tau_{xx}) + (\alpha_{IB} + \alpha_{PI}) I - \epsilon_{rad}. \end{aligned} \quad (6)$$

Here ρ denotes the total mass density of Cu and He in the plume, which is equal to $\rho_v + \rho_b$, where ρ_v and ρ_b are the Cu and He vapor mass density, respectively. v denotes the plume velocity, ρU is the local internal energy density, and P denotes the local pressure. $\omega_v = \rho_v / \rho$ is the Cu vapor mass density fraction, and τ_{xx} is one component of momentum flux tensor equal to $-(4/3)\mu(\partial v / \partial x)$. q represents the conductive and diffusive energy flux relative to the mass average velocity of the mixture. D_{ab} is the binary diffusivity of the mixture. The diffusion caused by pressure gradient and number density gradient is neglected here because it is much weaker than that due to the mass gradient. $I(x, t)$ is the laser irradiance, and α_{IB} and ϵ_{rad} are the linear light absorption coefficient in the inverse bremsstrahlung (IB) and the radiation power loss emitted in the bremsstrahlung process, respectively. α_{PI} is the light absorption coefficient due to the photoionization (PI) process.

The energy flux q is given below,

$$q = -(\lambda + \lambda_e) \frac{\partial T}{\partial x} - \sum H_i \rho D_{ab} \frac{\partial \omega_i}{\partial x}, \quad (7)$$

where λ is the thermal conductivity of atoms and ions in the binary mixture, λ_e is the electron thermal conductivity which is a function of electron number density and temperature and ion number densities as well as neutral atom number densities.³⁹ Even when the plume is weakly ionized, λ_e is typically larger than λ . H_i is the component enthalpy on a mass basis. D_{ab} is the binary diffusivity for the vapor-ambient system, defined by,³⁸

$$D_{ab} = \frac{2}{3} \left(\frac{k_B}{\pi} \right)^{3/2} \left(\frac{1}{2m_a} + \frac{1}{2m_b} \right)^{1/2} \frac{T^{3/2}}{P \left(\frac{d_a + d_b}{2} \right)^2}, \quad (8)$$

where k_B is the Boltzmann constant and $m_{a(b)}$ and $d_{a(b)}$ stand for the mass and diameter of Cu (He) atoms, respectively.

The thermal conductivity λ and the viscosity μ for the binary mixture are defined as follows:³⁸

$$\lambda = \sum_{i=1}^n x_i \lambda_i \bigg/ \sum_{j=1}^n (x_j \Phi_{ij}), \quad (9)$$

and

$$\mu = \sum_{i=1}^n x_i \mu_i \bigg/ \sum_{j=1}^n (x_j \Phi_{ij}), \quad (10)$$

where $\lambda_i = \sqrt{k_B^3 T / \pi^3 m_i} / d_i^2$, $\mu_i = \sqrt{m_i k_B T / \pi} / (\pi d_i^2)$, x_j is the number density fraction of the j th species, and Φ_{ij} is given as follows:

$$\Phi_{ij} = \frac{1}{\sqrt{8}} \left(1 + \frac{m_i}{m_j} \right)^{-1/2} \left(1 + \frac{d_j}{d_i} \right)^2. \quad (11)$$

In this paper we consider the ionization of Cu into Cu⁺ and Cu²⁺ and the ionization of He into He⁺. If the electrons have a Maxwellian velocity distribution, the total amount of energy emitted per unit volume per unit time is⁴⁰

$$\epsilon_{rad} = \left(\frac{2\pi k_B T}{3m_e} \right)^{1/2} \frac{32\pi e^6}{3hm_e c^3} n_e (n_{v1} + 4n_{v2} + n_{b1}), \quad (12)$$

where e is the electron charge, m_e is the electron mass, c is the velocity of light, and h is the Planck constant; n_e is the

local electron number density, n_{v1} and n_{v2} are the Cu^+ and Cu^{2+} number densities, respectively, and n_{b1} is the He^+ number density.

Assuming that the evaporated material and the background gas follow the ideal gas law, the local pressure and internal energy density can be expressed as

$$P = (1 + x_{e,v})n_v k_B T + (1 + x_{e,b})n_b k_B T, \quad (13)$$

$$\rho U = n_v \left[\frac{3}{2}(1 + x_{e,v})k_B T + \text{IP}_1 x_{i1} + (\text{IP}_1 + \text{IP}_2)x_{i2} \right] + n_b \left[\frac{3}{2}(1 + x_{e,b})k_B T + \text{IP}_{b1} x_{e,b} \right]. \quad (14)$$

Here, $x_{e,v}$, x_{i1} , and x_{i2} denote the partial fraction of electrons, singly charged ions (Cu^+), and doubly charged ions (Cu^{2+}) from Cu, they satisfy $x_{e,v} = x_{i1} + 2x_{i2}$; $x_{e,b}$ denotes the partial fraction of electrons from He, which is equal to the partial fraction of He^+ ions from He. IP_1 and IP_2 are the first and second ionization potential of Cu, respectively. IP_{b1} is the first ionization potential of He. $n_v = \rho_v/m_v$ and $n_b = \rho_b/m_b$ are the Cu number density and He number density, respectively.

Numerically, the system of equations, which describe the flow of mass, momentum, and energy, is solved using the first-order Godunov method (for the convective terms) and a first-order central difference method (for the diffusion, viscosity, and thermal conduction terms).

C. Plasma formation

When the first-order and second-order ionizations of Cu and the first-order ionization of He are considered, the Saha–Eggert equations are as follows:

$$\frac{(n_v x_{e,v} + n_b x_{e,b})x_{i1}}{1 - x_{i1} - x_{i2}} = \left(\frac{2\pi m_e k_B T}{h^2} \right)^{3/2} \exp\left(-\frac{\text{IP}_1}{k_B T}\right), \quad (15)$$

$$\frac{(n_v x_{e,v} + n_b x_{e,b})x_{i2}}{x_{i1}} = \left(\frac{2\pi m_e k_B T}{h^2} \right)^{3/2} \exp\left(-\frac{\text{IP}_2}{k_B T}\right), \quad (16)$$

$$\frac{(n_v x_{e,v} + n_b x_{e,b})x_{e,b}}{1 - x_{e,b}} = \left(\frac{2\pi m_e k_B T}{h^2} \right)^{3/2} \exp\left(-\frac{\text{IP}_{b1}}{k_B T}\right). \quad (17)$$

Here $n_v x_{e,v} + n_b x_{e,b} = n_e$ is the local electron number density of the two-component mixture.

The three Saha–Eggert equations are combined with one extra equation, i.e., for the conservation of charge for the Cu component,

$$x_{i1} + 2x_{i2} = x_{e,v}. \quad (18)$$

Finally, the vapor temperature (T) in the Saha–Eggert equations is adopted from the internal energy density [see Eq. (14) above]. These five equations [Eqs. (14)–(18)] are solved together to calculate the five unknown values ($x_{e,v}$, x_{i1} , x_{i2} , $x_{e,b}$ and T). The Newton–Raphson method was applied to solve this strongly nonlinear system of equations.

D. Laser absorption in the plasma

Because of the formation of a plasma in front of the target, the laser beam will be partially absorbed before it

reaches the target, i.e., so-called “plasma shielding.”³⁵ The three dominant mechanisms for absorption of visible or UV laser light in the Cu vapor are electron-ion and electron-neutral inverse bremsstrahlung and photoionization of excited atoms. The inverse bremsstrahlung absorption process involves the absorption of a photon by a free electron. The electron is raised to a higher state in the continuum. This process must occur within the field of a heavy particle (ion or neutral), so that momentum is conserved.⁴¹ At the laser intensity typically used in visible and UV laser-ablation experiments with nanosecond laser pulses ($I \approx 10^{12} - 10^{13} \text{ W/m}^2$), IB cross sections can reach values as high as 10^{-23} m^2 during the laser pulse. In visible and UV laser ablation of metals, the photon energy is mostly comparable with the typical ionization energy of excited atoms, making the photoionization cross section of the order of 10^{-21} m^2 in most cases. In the paper, we have adopted 10^{-21} m^2 as the PI cross section σ_{PI} in the calculations. So, the absorption coefficient α_{PI} may be approximately estimated as $\sigma_{\text{PI}} n_v$.

The two contributions to inverse bremsstrahlung are electron-neutral and electron-ion inverse bremsstrahlung, which are given by,⁴²

$$\alpha_{e,n} = [1 - \exp(-h\nu/k_B T)] Q n_e n_0, \quad (19)$$

and

$$\alpha_{e,i} = \left[1 - \exp\left(-\frac{h\nu}{k_B T}\right) \right] \frac{4e^6 n_e}{3hc\nu^3 m_e} \left(\frac{2\pi}{3m_e k_B T} \right)^{1/2} \times (n_{v1} + 4n_{v2} + n_{b1}), \quad (20)$$

where ν is the laser frequency, n_0 is the local neutral number density (Cu+He), and Q is the cross section of the photon absorption.⁴² The total absorption coefficient α_{IB} is equal to $\alpha_{e,n} + \alpha_{e,i}$. Assuming that the original laser irradiance is $I_0(t)$, the laser irradiance after plasma shielding $I(x, t)$ can be obtained by $I(x, t) = I_0(t) \exp[\int_x^\infty (\alpha_{\text{IB}} + \alpha_{\text{PI}}) dx]$.

E. Boundary conditions

The heat conduction equation, Eq. (1), is accompanied by one initial and two boundary conditions,²⁴

$$T(t, z) = T_a, \quad \text{at } t = 0, \quad (21)$$

$$T(t, z) = T_a, \quad \text{at } z \rightarrow \infty, \quad (22)$$

$$v(n_v \Delta H_{lv} + \rho U + \rho v^2/2 + P) - \lambda \frac{\partial T(t, z)}{\partial z} = (1 - R_f)I(t), \quad \text{at } z = 0, \quad (23)$$

where T_a is the ambient temperature and ΔH_{lv} is the heat of vaporization. Equation (23) is the energy balance at the target surface, which couples the heat conduction and the gas-dynamic equations. The velocity of surface recession $u(t)$ is defined by the mass balance,

$$N_c u(t) = n_v v, \quad \text{at } x = 0, \quad (24)$$

where N_c is the Cu number density in solid state.

The initial conditions for the gas-dynamic equations, Eqs. (3)–(6), are determined by the ambient pressure P_a and temperature T_a ,

$$\{T = T_a, P = P_a, n_v = 0, v = 0\}, \quad \text{at } t = 0. \quad (25)$$

To obtain the required boundary conditions, the characteristic equations following from Eqs. (3)–(6) should be considered.²⁴ The number of boundary conditions is equal to the number of independent variables transferred along the characteristics incoming into the volume from the boundary surface under consideration.⁴³ As was discussed in Ref. 43, for one-dimensional nonsteady flow, there are three sets of characteristics: C_+ [$(dx/dt)_+ = v + C$], C_- [$(dx/dt)_- = v - C$], and C_0 ($dx/dt = v$), where C is the sound velocity. In the two-component case under consideration there are four independent characteristic variables.²⁴ They may be introduced as two Riemann invariants (one transferred along the C_+ characteristics and the other one transferred along the C_- characteristics), entropy, and relative vapor concentration (both transferred along the C_0 characteristics). At infinity only the C_- characteristics are incoming and therefore one condition is sufficient,

$$P \rightarrow P_a, \quad \text{at } x \rightarrow \infty. \quad (26)$$

At the evaporated target surface the C_0 and C_+ characteristics are incoming and hence three boundary conditions are to be specified. One of them is the inert gas flux,

$$n_b v = 0, \quad \text{at } x = 0, \quad (27)$$

and the two others are to be determined by the vaporization kinetics, as described below.

At the target surface, the gas near the phase boundary is not in translational equilibrium when the evaporation rate is large. To realistically represent the conditions at the target-flow boundary, a Knudsen layer model is employed, which treats that region as a gas-dynamic discontinuity across which certain jump conditions, expressing conservation of mass, momentum, and energy, are applied. Translational equilibrium is achieved within a few mean free paths by collisions between particles in the Knudsen layer region. Changes in flow properties can be described as jump conditions across the Knudsen layer, simplified for a monatomic gas ($\gamma = 5/3$),⁴⁴

$$\left(\frac{T_k}{T_s}\right)^{1/2} = \left(1 + \frac{\pi s^2}{64}\right)^{1/2} - \frac{\pi^{1/2}}{8} s, \quad (28)$$

$$\frac{P_k}{P_s} = \left(\frac{T_k}{T_s}\right)^{1/2} \left[\left(s^2 + \frac{1}{2}\right) \text{erfc}(s) \exp(s^2) - \frac{s}{\pi^{1/2}} \right] + \frac{1}{2} [1 - \pi^{1/2} \text{erfc}(s) \exp(s^2)], \quad (29)$$

where $T_k = T(0, t)$ and $P_k = P(0, t)$ are the temperature and pressure at the outer edge of the Knudsen layer, respectively, the target surface temperature T_s equals $T(t, x = 0)$ and the saturation pressure P_s is calculated by Eq. (2). $s = u_k / (2k_B T_k / m_v)^{1/2}$ is the speed ratio, where u_k is the velocity at the outer edge of the Knudsen layer.

The Cu vapor density at $x = 0$, $n_v(0, t)$, is assumed to be equal to the Cu vapor number density at the outer edge of the Knudsen layer, n_k , which can be obtained from T_k and P_k . At the Chapman–Jouguet point where the vaporization speed approaches the sound speed [$u_k = C_k = (\gamma k_B T_k / m_v)^{1/2}$], the gas-dynamic disturbances cannot reach the target surface and therefore influence the vaporization kinetics.²⁴ Further increasing the vapor velocity and reducing the pressure below this point appear to be impossible.

When the surface temperature T_s decreases, the saturation pressure P_s also drops down, thus it may become less than the vapor pressure at the outer edge of the Knudsen layer P_k , and back condensation may start to occur. The boundary value of the gas velocity for the case of back condensation is negative, only the C_+ characteristics are incoming, and one boundary condition is required. The condensation flux is defined by the Hertz–Knudsen equation,²⁴

$$n_k u_k = \frac{P_s - P_k}{(2\pi m_v k_B T_s)^{1/2}}, \quad (30)$$

which is applied when the saturation pressure P_s becomes lower than the gas pressure P_k . It should be pointed out that, when the ionization and laser absorption by the plasma is taken into account, the back condensation process may occur before the laser pulse is terminated. Indeed, when the plasma is formed, the plasma shielding plays a role so that the laser irradiance impinging on the target surface is lower than that for the case of no plasma shielding, resulting in a faster decrease of the surface temperature and saturation pressure.

F. Coupling of the different parts of the model

The different parts of the model are strongly coupled. During the laser pulse, on one hand, the laser-target interaction, which leads to the heating of the target and evaporation, needs information from the plume part to fix its boundary condition [see Eq. (23)]. On the other hand, the boundary condition for the plume part needs information from the target surface as well, i.e., the evaporation flux. Moreover, after the laser pulse is finished or the evaporation stops, the contribution of back condensation to the target heat conduction is also considered in this model, thus the plume affects the target again. Furthermore, the absorption of the laser beam in the plasma represents an important coupling back, both to the plume expansion (gain and loss terms in the equation for conservation of energy), and to the laser-solid interaction, because the laser energy can be considerably attenuated (plasma shielding) before it reaches the target, leading to less efficient target heating, melting, and vaporization.

Therefore, the different parts of the model need to be solved simultaneously as a function of time, in order to obtain an overall picture of the mechanism of laser ablation of a Cu target, plume expansion in the background gas He, and plasma formation.

III. NUMERICAL RESULTS AND DISCUSSIONS

The calculations are performed for a Gaussian-shaped laser pulse with wavelength of 266 nm, full width at half maximum (FWHM) of 10 ns, and peak laser irradiance of

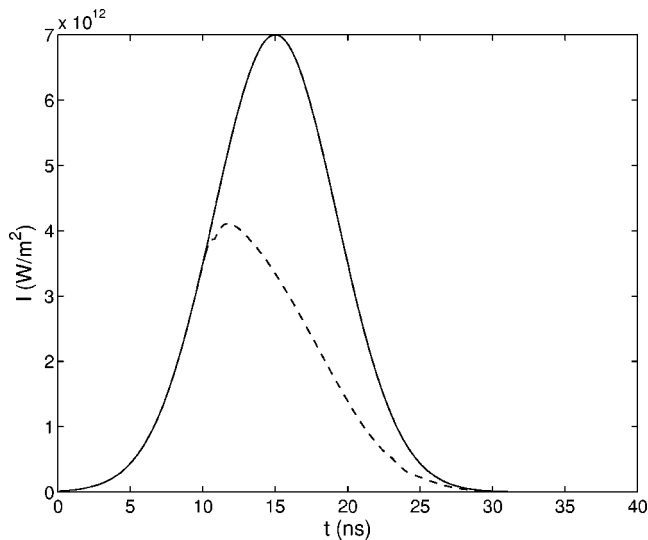


FIG. 1. Laser intensity-time profile assumed in the model. It is a Gaussian-shaped pulse with 10-ns full width at half maximum and peak irradiance of 7×10^{12} W/m². The solid line represents the original laser pulse and the dashed line represents the calculated laser irradiance arriving at the target, after passing through the plume (plasma).

7×10^{12} W/m² (see Fig. 1, solid line). Integrated over the entire pulse, this yields a fluence of 74.2 kJ/m². In the calculations, we follow only one laser pulse. The dashed line in Fig. 1 shows the laser irradiance arriving at the target, after passing through the plume. It is clear that the laser irradiance at the target drops significantly after about 12 ns, as a result of plasma shielding of the original laser pulse. After this plasma shielding, the laser irradiance impinging on the target is at maximum only about 4.2×10^{12} W/m². This result is quite similar to the case of laser ablation of Cu in vacuum.³⁰

A. Target heating, melting, and vaporization

The Cu target is initially at room temperature T_a . However, as a result of laser energy deposition on the target, the target is heated very quickly. The calculated temperature distribution in the target is plotted as a function of time during and after the laser pulse in Fig. 2(a). The temperature is at maximum at the surface of the target, as expected. The maximum temperature of about 8000 K is reached between 14 and 16 ns. When time evolves, the region with elevated temperature (i.e., above room temperature) expands due to thermal conduction. For the conditions under consideration, the heating is more or less limited to the first 10 μm of the target. As far as melting is concerned, only a few micrometers are influenced, as appears from Fig. 2(b). Although the surface temperature drops significantly when the laser absorption is very strong, the first 2 μm of the target still remains in a molten phase for quite a long time. Only after approximately 70 ns, resolidification of the melt starts to occur, and the melt depth starts to drop very slowly.

Figure 3 shows the surface recession rate and the evaporation depth as a function of time. It is clear that the evaporation rate reaches a maximum (of about 6.8 m/s) at about 15 ns, i.e., when the target surface temperature is at the maximum (about 8000 K). One can see from the surface recession rate that the evaporation process stops at about

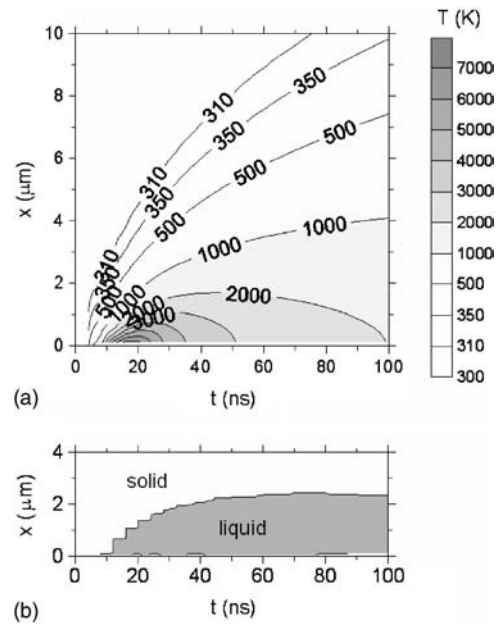


FIG. 2. Temporal evolution of (a) calculated temperature distribution in the target and (b) calculated solid/liquid regions in the target, for the conditions shown in Fig. 1. The original target surface is at 0 μm .

25 ns. As was shown in Fig. 1, the laser absorption by the plume starts at about 10 ns, and during the following 15 ns, the plume is ionized to form a plasma above the target surface. The huge pressure of the formed plasma may prevent the evaporation process from the target surface [see Eq. (30)]. As a consequence, the competition between the evaporation and the back condensation on the target surface reaches a more or less stable state from 25 to about 40 ns. This means neither evaporation nor reconcondensation happens during the time period. The similar phenomenon was reported in Ref. 25. One could see that the surface recession rate is zero during this time period although there is a little oscillation in the recession rate. Meanwhile, the depth of evaporation does not change either. After 40 ns, the saturated pressure becomes lower than the pressure of the plume

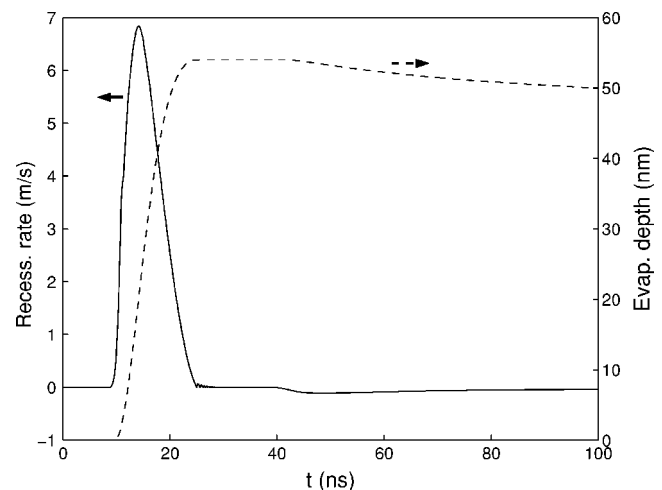


FIG. 3. Calculated surface temperature (solid line, left axis) and calculated depth of evaporation (dashed line, right axis) as a function of time, for the conditions shown in Fig. 1.

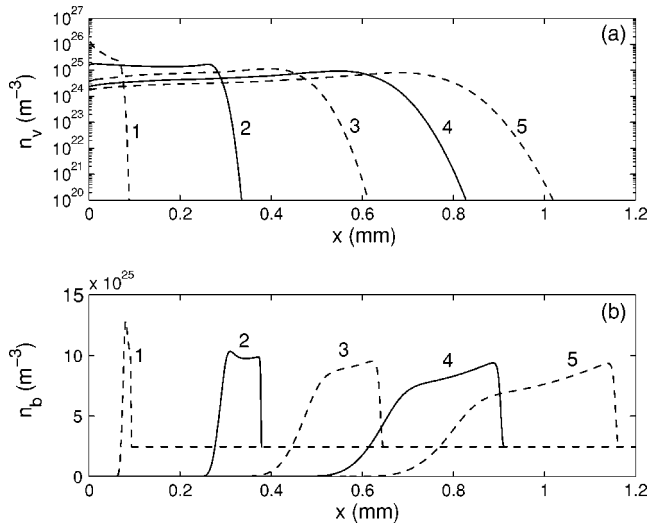


FIG. 4. Spatial distribution of (a) calculated Cu number density and (b) calculated He number density in the plume, at different times: 20 (1), 40 (2), 60 (3), 80 (4), and 100 ns (5), for the conditions shown in Fig. 1.

nearly by the surface, due to the quick drop of the surface temperature. From this moment on, the true recondensation onto the target surface starts. One may notice that the depth of evaporation is quite similar to that for the case of ablation in vacuum (see Ref. 30 and the references therein) although in the latter case a somewhat higher laser irradiance (10^{13} W/m^2) was used. Comparing Figs. 2 and 3, one can see that the evaporation process affects only the surface layer, till a depth which is a factor of 30 smaller than the depth at which melting takes place.

B. Plume expansion and plasma formation

Figure 4 shows the calculated Cu vapor and background gas number densities at different times. One can see that, at an early stage of the ablation, for example, at 20 ns, the Cu vapor density is highest at the target (almost $4 \times 10^{26} \text{ m}^{-3}$), it drops gradually as a function of distance away from the target surface in the plume, and very rapidly at the plume front. When time evolves, the situation has changed, i.e., the Cu vapor density is highest in the plume instead of at the target. For example, at 40 ns, the maximum value of the Cu vapor density n_v drops down to about $2.1 \times 10^{25} \text{ m}^{-3}$, and is located at about 0.05 mm from the target. This is because the plume becomes longer as time evolves but the material evaporation from the target decreases quickly when the laser pulse is finished. When the time evolves further, the plume size increases. Accordingly, the maximum value of Cu vapor density decreases along with time since the vapor expands into a bigger space but there is no material supply after the evaporation process stops. For example, at 100 ns, the maximum value of Cu vapor density drops to $8 \times 10^{24} \text{ m}^{-3}$ and its location is about 0.72 mm away from the surface.

Meanwhile, in Fig. 4(b) one can see that the background gas He is gradually pushed away by the Cu vapor, forming a compression shock wave. The highest value of He number density n_b can be as large as $1.24 \times 10^{26} \text{ m}^{-3}$ at 20 ns. Note that the value of He number density corresponding to 1 atm at room temperature is only $2.45 \times 10^{25} \text{ m}^{-3}$. According to

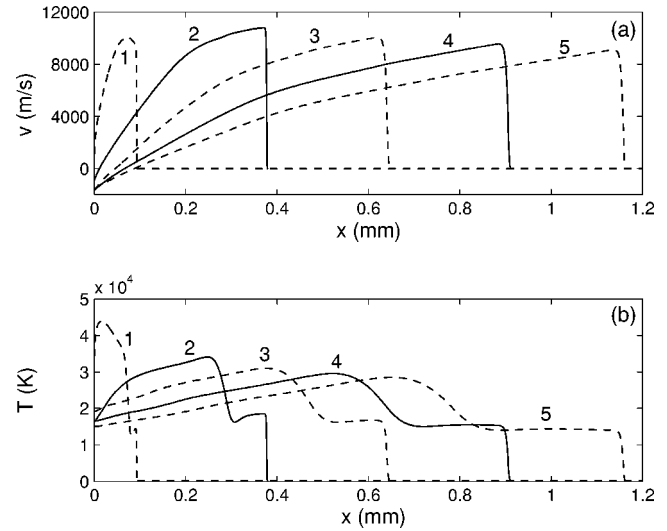


FIG. 5. Spatial distribution of (a) calculated plume velocity and (b) calculated plume temperature, at different times: 20 (1), 40 (2), 60 (3), 80 (4), and 100 ns (5), for the conditions shown in Fig. 1.

the so-called Sedov shock wave theory (e.g., see Ref. 45), the ratio of the number density just at the shock front to that in the undisturbed region is $(\gamma+1)/(\gamma-1)$. When $\gamma=5/3$, this ratio equals 4. Our calculated number density ratio during the laser pulse-on period is about 5, which is somewhat larger than the predicted value of 4. This is because there is always an extra material and energy added to the plume during the pulse-on period, which is not accounted for in the Sedov shock wave theory. When the pulse has passed, the number density ratio will gradually drop to the ideal value of 4.

Figure 5(a) presents the plume velocity v distribution at different times. The plume expansion into 1-atm background gas is expected to be slower than the expansion into vacuum. When the laser pulse is finished (at approximately 30 ns), the maximum velocity is less than 10 000 m/s. At 40 ns, the velocity of the shock wave reaches 10 700 m/s. In the experiment of Harilal *et al.*,⁴ the laser ablation plume of Al into ambient air with pressure ranging from 10^{-6} to 100 Torr was studied, using a Nd:YAG (yttrium aluminum garnet) laser (8-ns pulse width, maximum energy 700 mJ). For the case of 100 Torr ambient air, they measured a maximum plume expansion velocity of about 10 000 m/s, which is very similar to our simulated result. In the vacuum case, the corresponding value is calculated to be about 25 000 m/s.³⁰ This shows indeed that the existence of the background gas greatly reduces the plume velocity and thus the plume expansion is confined to a smaller region. On the other hand, the plume expansion with the presence of ionization is faster than that without ionization. This can be seen from Ref. 25, in which the maximum plume velocity is only about 3000 m/s, although similar conditions were applied. Furthermore, if there is no ionization, the maximum temperature always locates at the front of the shock wave, as was reported in Ref. 25. However, because of laser absorption in the plume due to the existence of electrons and ions, the peak of temperature is shifted to the center part of the plume and its value can be much higher than that at the shock wave front.

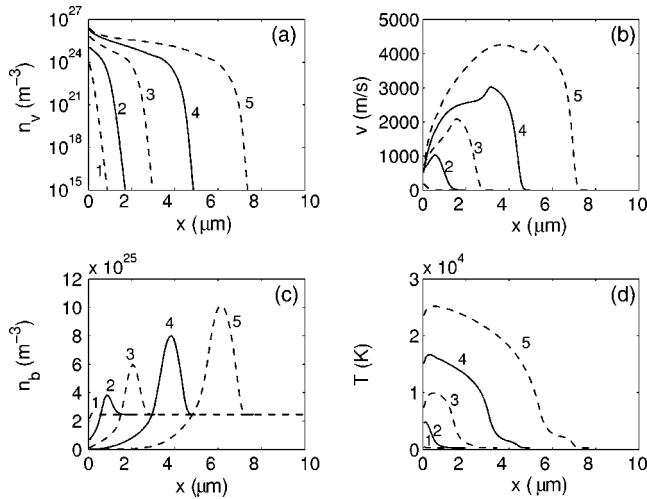


FIG. 6. Spatial distribution of (a) calculated plume velocity and (b) calculated plume temperature, at different times: 9 (1), 9.6 (2), 10.2 (3), 10.8 (4), and 11.4 ns (5), for the conditions shown in Fig. 1.

It should be pointed out that, even when the laser pulse is not finished, because of strong plasma shielding, the laser irradiance arriving at the target is so small that the surface temperature drops down dramatically. In this case, one can see from Eq. (30) that the flux will be directed toward the target and the plume velocity at the surface is negative. Considering this recondensation on the target surface, the plume velocity at the surface can be represented by the local sound speed. However, most of the plume is still moving away from the target, to push the background gas, although the plume front velocity decreases along with time (e.g., at 100 ns, the plume front velocity is only about 9000 m/s).

The temperature distribution in the plume is presented in Fig. 5(b). For the condition under consideration here, ionization is observed to occur after 9 ns, and photoionization of Cu may take a major role to start the ionization process. Subsequently, the plume can absorb energy directly from the laser beam due to IB and PI processes, which causes the plume temperature to increase further, resulting in fast ionization of the plume. At 20 ns, the maximum temperature in the plume can reach values as high as 42 000 K. As expected, the plasma continues to absorb energy from the laser beam during the pulse period. At 30 ns, the highest temperature in the plasma can be higher than 45 000 K (which is not shown here). After the laser extinguishes, the temperature of the plasma drops gradually. This is because the plasma drives the shock wave moving forward to push the ambient gas away and releases some energy into environment by bremsstrahlung radiation.

Figure 6 presents the calculated Cu vapor and background gas number densities, the calculated plume velocity, and the calculated plume temperature at different times, from 9 to 11.4 ns, i.e., around the time when the plasma is formed. At 9 ns, the evaporation is so weak that the Cu vapor number density is only about 10^{24} m^{-3} , even close to the target surface. The maximum temperature of the plume at this moment is only about 500 K. The background gas is pushed away slightly. As soon as the laser absorption starts (i.e., at 9.6 ns), the plume is heated up to a temperature of

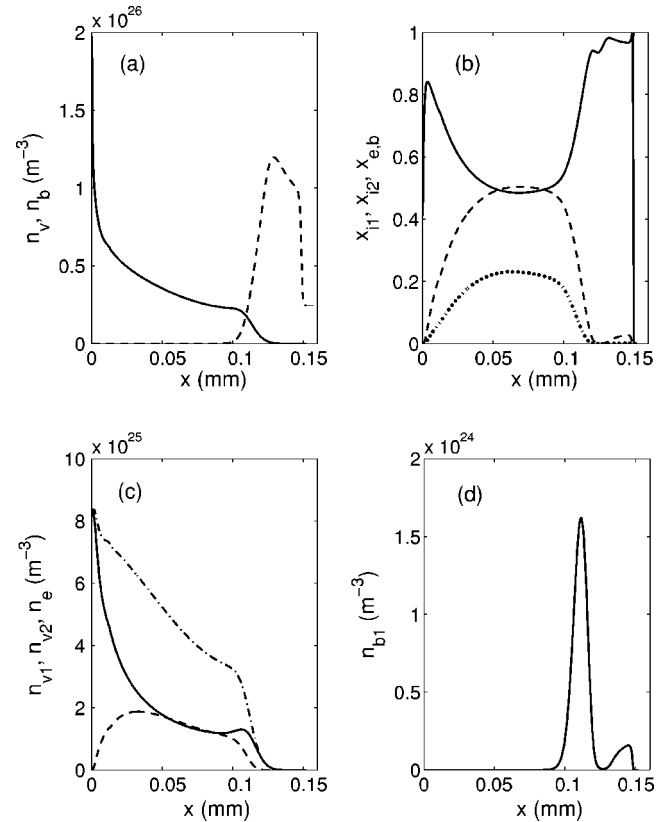


FIG. 7. Spatial distribution of (a) calculated Cu vapor density (solid line); calculated He density (dashed line); (b) calculated ionization degrees x_{i1} (solid line), x_{i2} (dashed line), and $x_{e,b}$ (dotted line); (c) calculated number density of Cu^+ (solid line); calculated number density of Cu^{2+} (dashed line); calculated number density of electron n_e (dashed-dotted line); and (d) calculated number density of He^+ at 24 ns, for the conditions shown in Fig. 1.

about 10 000 K at 10.2 ns. Then the thermal ionization of Cu also occurs. At 11.6 ns, the plume is already converted into a plasma. Accordingly, the plume velocity is increased dramatically to 4500 m/s. Figure 6(c) shows how the compression shock wave is developed from 9 to 11.6 ns.

Figure 7(a) shows the spatial distribution of Cu and He number densities at 24 ns, i.e., just before the evaporation stops. One can see that the peak of Cu vapor number density is still adjacent to the target surface. However, the background gas He is pushed away to form a very distinct peak in the number density (about five times the number density in the undisturbed region). A layer of interpenetration or mixing between Cu vapor and ambient gas is also clearly observed. For convenience to discuss the ionization of the plasma, here we would like to call this layer the mixing layer. At 24 ns, the thickness of the mixing layer is about $20 \mu\text{m}$, which corresponds to 200 spatial grids in our simulations.

Figure 7(b) shows the spatial distribution of the ionization degree of Cu and He at 24 ns. The plume behavior highly depends on space. Hence, to analyze the ionization of the plume more clearly, we divide for convenience the whole region where Cu vapor mainly exists into three parts: region C (i.e., the central part of the plume, which will be referred to below as the “core”), region M (or the mixing layer where the Cu vapor and the He gas exist together), and region S (close to the target surface). Notice that the size of each

region may vary with time. At 24 ns, region C is located from 20 to 90 μm , region M is located from 90 to 130 μm , and region S from 0 to 20 μm . First, in region C, the temperature is the highest among the three regions. More than half of the Cu vapor is ionized into Cu^{2+} ions, and the whole ionization degree of Cu ($x_{i1}+x_{i2}$) is greater than 0.99, which means a highly ionized plasma. Second, in region M, the first-order and the second-order ionization degrees of Cu are about 0.6 and 0.2, respectively; the ionization degree of He is about 0.1. Finally, in region S, it is clear that the first-order ionization of Cu dominates and the maximum of x_{i1} is 0.85.

It should be emphasized that it does not make sense to discuss the ionization degree of He in region C and region S because there is almost no He observed in these two regions. All He atoms are pushed to region M and the shock region.

Figure 7(c) presents the spatial distribution of Cu^+ (n_{v1}), Cu^{2+} (n_{v2}), and electron (n_e) number densities at 24 ns. The maximum Cu^+ ion number density is about $8.5 \times 10^{25} \text{ m}^{-3}$ and is located near the target surface. In region C, one can see that the number densities of Cu^+ and Cu^{2+} are almost equal. The electron number density is almost equal to the sum of these two because the contribution of He is negligible here. Figure 7(d) shows the spatial distribution of He^+ number density at 24 ns. In region M, the density of He^+ ions reaches a maximum of $1.6 \times 10^{24} \text{ m}^{-3}$. Just behind the shock wave front, the number density of He^+ is about $2 \times 10^{23} \text{ m}^{-3}$ due to the shock heating effect. Compared to Fig. 7(c), one can see that the contribution of He ionization to the electron production is absolutely weak. In experiments, under the condition of 1-atm He background gas, the ionization and the presence of electrons are indeed observed. For example, Detalle *et al.*¹¹ studied a 6 ns laser pulse at 1064 nm on an Al target in He background gas, for a laser irradiance of about $3.7 \times 10^8 \text{ W/cm}^2$. They measured an electron density of about $7 \times 10^{23} \text{ m}^{-3}$ at 50 ns and a corresponding temperature of around 10 000 K. This is lower than our calculated values, but this is as expected because of the lower laser irradiance.

Figure 8(a) presents the absorption coefficients $\alpha_{e,n}$ and $\alpha_{e,i}$ as well as α_{PI} at 12 ns (a) and 24 ns (b). At 12 ns, one can clearly see that the PI and the electron-neutral IB absorption mechanisms are more important than electron-ion IB absorption within the whole plume. This is because the ionization just starts and the electron number density is still low, but the neutral atom number density is very high. Hence, the electron-ion collision cross section is much lower than the other two cross sections. However, at later time, the different absorption mechanisms may compete with one another. For example, at 24 ns, as is shown in Fig. 8(b), the absorption mechanism depends on the location in the plume. In the whole region, the electron-neutral IB absorption is the most important. Besides, from the target surface to 0.045 mm, the PI absorption is stronger than the electron-ion IB absorption. In the rest of the plume, the situation is reversed. This can be explained as follows. When the plasma is initially formed, the photoionization plays a major role. Subsequently when the plasma is formed, no matter how high the ionization degree is, the electron-neutral IB absorption starts to play an important role because the plasma is confined within a

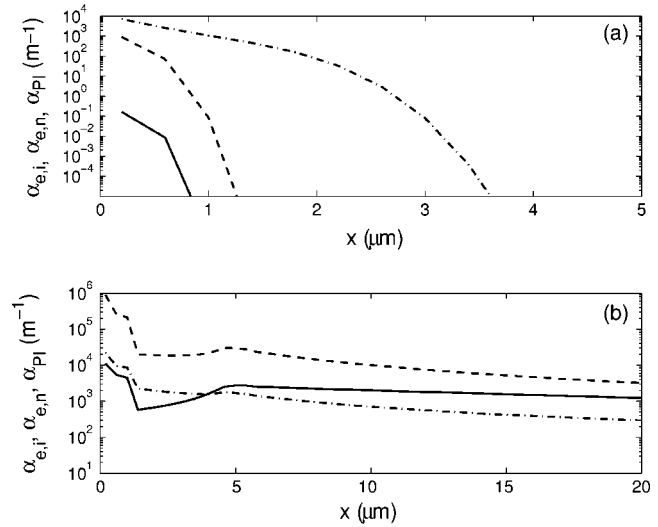


FIG. 8. Spatial distribution of absorption coefficients $\alpha_{e,i}$ (solid line), $\alpha_{e,n}$ (dashed line), and α_{PI} (dashed-dot line). (a) is at 12 ns and (b) is at 24 ns, for the conditions shown in Fig. 1.

smaller region due to the plume expansion into a very dense ambient gas. In the region where the plasma is highly ionized, thus the electron-ion IB absorption becomes important but never dominates. This is the way of how the plume under consideration evolves into a plasma.

To study the effect of laser irradiance on the laser ablation of Cu into 1-atm ambient gas, we have varied the laser irradiance from 1×10^{12} to $9 \times 10^{12} \text{ W/m}^2$. Figure 9 presents the maximum of the surface temperature as a function of laser irradiance. The surface temperature increases smoothly with laser irradiance, but a small discontinuity in the slope is observed at about $1.9 \times 10^{12} \text{ W/m}^2$. When the laser irradiance is lower than this value, the maximum of the surface temperature increases more quickly than when the laser irradiance is higher than this value. From Fig. 9(b) it appears that the depth of evaporation has a similar but opposite behavior. With laser irradiances below $1.9 \times 10^{12} \text{ W/m}^2$, the evaporation depth is very small and increases only slowly with laser irradiance. Above the threshold value, the evaporation depth increases more quickly with laser irradiance. Considering the laser pulse duration used in our simulations, it follows that $1.9 \times 10^{12} \text{ W/m}^2$ irradiance corresponds to 20.6 kJ/m^2 (or 2.06 J/cm^2) laser fluence. The fraction of laser energy absorbed by the plume versus laser irradiance is given in Fig. 9(c). Once again a different behavior is clearly observed before and after the irradiance of $1.9 \times 10^{12} \text{ W/m}^2$. This threshold value for the plasma formation is surprisingly close to that in the vacuum case. It is reported in Ref. 46 that in the nanosecond laser ablation of metals in vacuum, for fluences higher than the fluence threshold ($F \geq 2 \text{ J cm}^{-2}$), a plasma is always produced above the target surface.

Figure 10 shows the effect of the laser irradiance on the calculated ionization fraction of Cu and He in the core part of the plasma (a) and in the mixing layer (b). Except for the laser irradiance, the other laser parameters (wavelength, pulse shape, and duration) are kept constant. The spatial and temporal behaviors of the formed plasma will be somewhat

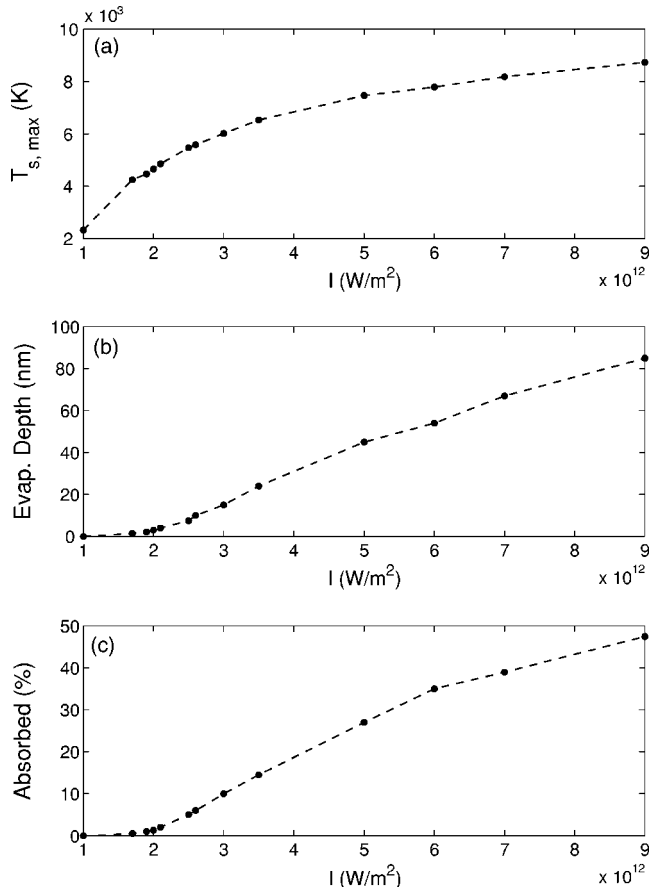


FIG. 9. Laser irradiance dependence of (a) calculated maximum surface temperature, (b) calculated evaporated depth, and (c) calculated fraction of the laser energy absorbed by plasmas. All laser pulses have the same parameters except for laser irradiance.

different for different values of laser irradiance. However, in order to make a comparison possible, we focus on the ionization of Cu and He at 30 ns, i.e., when the laser pulse is finished. It is clear that in the core part of the plasma, the first-order ionization of Cu first increases with the laser irradiance. However, when the laser irradiance increases above $3 \times 10^{12} \text{ W/m}^2$, the second-order ionization of Cu also becomes important, and consequently the fraction of the first-order ionization of Cu starts to decrease almost linearly along with the irradiance. At the same time, the second-order ionization of Cu in the core of the plasma increases monotonously with laser irradiance. At about $7 \times 10^{12} \text{ W/m}^2$, both fractions are more or less equal, and for higher laser irradiance, the second-order ionization of Cu even dominates over the first-order ionization of Cu. In the mixing layer, the situation is a little different. The first-order ionization of Cu again increases the irradiance of $3 \times 10^{12} \text{ W/m}^2$. Then it stays almost constant when the irradiance rises up to $5 \times 10^{12} \text{ W/m}^2$. Subsequently, it starts dropping gradually with the increase of laser irradiance. From 7 to $9 \times 10^{12} \text{ W/m}^2$, the first-order ionization of Cu again decreases with the laser irradiance slightly. The second-order ionization of Cu always increases with the laser irradiance between 2 and $9 \times 10^{12} \text{ W/m}^2$. However, from 7 to $9 \times 10^{12} \text{ W/m}^2$, the second-order ionization of Cu increases with the laser irradiance only slightly. The ionization of He

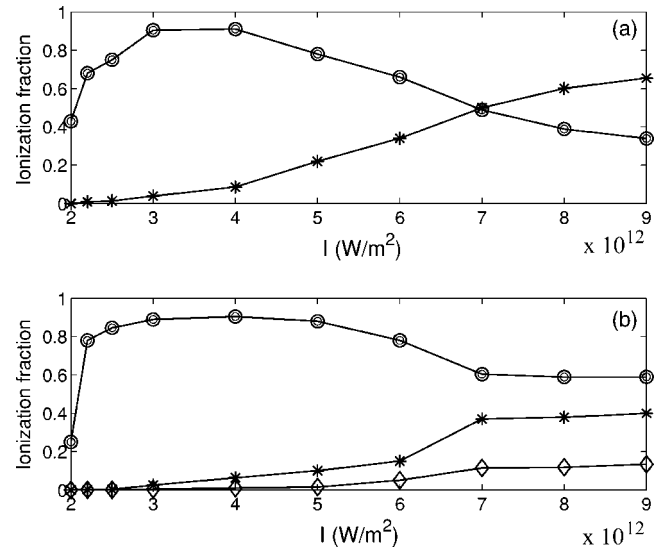


FIG. 10. Calculated ionization fractions of Cu^+ (circles), Cu^{2+} (asterisks), and He^+ (diamonds) (a) in the core part of the plasma and (b) in the mixing layer, as a function of laser irradiance at 30 ns. All laser pulses have the same parameters except for laser irradiance. The ionization of He is only considered in the mixing layer, as shown in (b).

reaches a maximum fraction of about 0.13 at $9 \times 10^{12} \text{ W/m}^2$. However, the contribution of He ionization to the total electron number density is very small because the He number density in the mixing layer is not large (around 10^{25} m^{-3}) and the mixing layer is very thin compared to the whole plume, as was shown in Fig. 7.

It is clear from Fig. 10, that even at a lower irradiance of $2 \times 10^{12} \text{ W/m}^2$, the ionization degree of Cu is still more than 42% in the core of the plasma and 25% in the mixing layer. For higher irradiances, the total ionization fraction of Cu can be more than 98%, which indicates that a highly ionized plasma is formed during the plume expansion.

IV. CONCLUSION

In summary, we have presented a one-dimensional model for the laser ablation of a Cu target into 1-atm background gas He. The heat conduction of the target is studied with the inclusion of the back flux. Binary diffusion, viscosity, and thermal conduction including the electron thermal conduction are taken into account in the evaporated plume. The ionization of Cu and He in the plume and the laser absorption by the plume were also simulated. The ionization of Cu and He enables the recondensation at the target surface to happen even during the laser pulse. The simulations have shown that the ionization degrees of Cu and He may vary greatly with the location in the plume. It was shown that at the conditions under consideration (a laser pulse with $7 \times 10^{12} \text{ W/m}^2$ peak irradiance, 266-nm wavelength, and 10-ns FWHM), the first-order ionization of Cu dominates in the region close to the surface, and the second-order ionization degree of Cu is a little bit higher than the first-order ionization degree of Cu in the core part of the plume. Both ionization degrees are close to 0.5, which means that the core of the plume becomes a nearly fully ionized plasma. In the mixing layer, the first-order ionization of Cu is more impor-

tant than the second-order ionization. The calculated ionization of He in the mixing layer has an average fraction of 0.08 and its contribution to the electron density is of the order of 10^{24} m^{-3} only in the mixing layer. In the core part of the plume, although the calculated ionization degree of He is as high as 0.2, there are very few electrons arising from the ionization of He due to the very low number density of He atoms. Hence, the ionization degree of 0.2 does not have true influence on the dynamics.

The plume expansion is greatly influenced by the presence of ionization and laser absorption in the plume. Comparing the simulated plume expansion velocity with that without considering ionization, we have found that the ionization and laser absorption indeed increase the plume expansion velocity because a part of the absorbed energy from the laser can be transferred into expansion motion. In our simulations, a maximum velocity of 10 000 m/s at the shock wave front is obtained. We have tried to make a comparison with experimental data, wherever it was possible. However, the experimental determination of the plasma parameters during the early times of laser ablation and plume expansion appears to be difficult because of the high optical thickness of the spectral lines emitted from the initial dense plasma. Due to the lack of available experimental data about the temperature and vapor number density at the early stages of laser ablation and plume expansion into 1-atm background gas, we could not present here a direct comparison of our numerical results with experiment. For the same reason, this indicates how valuable such modeling calculations can be, because they can give insight in the plume dynamics and plasma behavior, which is sometimes difficult to obtain from experiments.

Several absorption mechanisms are distinguished at different stages of plume expansion. The PI process and the electron-neutral IB process are important in the whole plume starting from the moment when the plume just begins to be ionized. At later time, the electron-neutral IB process is generally the most important everywhere in the plume except in the almost fully ionized plasma core. The PI is still more important than the electron-ion IB process in the region close to the target surface, but electron-ion IB becomes more important than PI further away from the surface. Furthermore, a threshold laser irradiance for the ablation rate and the plasma formation is found to be in a good agreement with that for the case of nanosecond laser ablation of metals in vacuum.

The effect of laser irradiance on the plasma has been studied as well. The results showed that there is a competition between the first-order and the second-order ionizations. In the core part of the plasma, the first-order ionization of Cu is more important than the second-order ionization when the laser irradiance is lower than $7 \times 10^{12} \text{ W/m}^2$; whereas for higher irradiances, the situation is reversed, i.e., the second-order ionization dominates over the first-order ionization. In the mixing layer, the first-order ionization of Cu is always more important than the second-order ionization although the latter one increases monotonously with laser irradiance. The ionization of He atoms is only important in the mixing layer

because there are not much He atoms in the core of the plasma. A calculated maximum He ionization fraction of about 0.13 is obtained at $9 \times 10^{12} \text{ W/m}^2$.

This model is primarily intended to describe LA for chemical analysis applications, such as LIBS and as a sample introduction method for ICPs, where the background gas is generally at 1 atm. However, the results are also applicable to other applications, such as PLD, where the background gas is at low pressure, and for obtaining more fundamental insight in the effect of a background gas. The model works from the stage of a plume without any ionization to that of a fully ionized plasma. This suggests that there may be some other applications in laser ablation where the ionization process needs to be considered. In future work, we plan to refine our model by extending it to two dimensions for the later stages of plume expansion.

ACKNOWLEDGMENTS

The authors thank A. Vertes, A. V. Gusarov, H. Deconinck, J. Deconinck, and G. Nelissen for many interesting discussions. This work was financially supported by the Flemish Fund for Scientific Research (FWO) and the IUAP-V project.

¹M. Von Allmen, *Laser Beam Interactions with Materials* (Springer, Heidelberg, 1987).

²D. B. Chrisey and G. K. Hubler, *Pulsed Laser Deposition of Thin Films* (Wiley, New York, 1994).

³A. G. Gnedovets, A. V. Gusarov, and I. Smurov, *J. Phys. D* **32**, 2162 (1999).

⁴S. S. Harilal, C. V. Bindhu, M. S. Tillack, F. Najmabadi, and A. C. Gaeris, *J. Appl. Phys.* **93**, 2380 (2003).

⁵H. W. Kroto, J. R. Heath, S. C. O'Brien, R. F. Curl, and R. E. Smalley, *Nature (London)* **318**, 162 (1985).

⁶L. J. Rakziemski, *Spectrochim. Acta, Part B* **57**, 1109 (2002).

⁷R. E. Russo, *Appl. Spectrosc.* **49**, 14A (1995).

⁸D. Günther, S. E. Jackson, and H. P. Longrich, *Spectrochim. Acta, Part B* **54**, 381 (1999).

⁹R. E. Russo, X. Mao, and S. S. Mao, *Anal. Chem.* **74**, 70A (2002).

¹⁰Yu. I. Koptev, *Gas Dynamics* (Nova Science Publishers, New York, 1992).

¹¹V. Detalle, M. Sabsabi, L. St-Onge, A. Hamel, and R. Héon, *Appl. Opt.* **42**, 5971 (2003).

¹²I. NoorBatcha, R. R. Lucchese, and Y. Zeiri, *J. Chem. Phys.* **86**, 5816 (1987).

¹³D. Sibold and H. M. Urbassek, *J. Appl. Phys.* **73**, 8544 (1993).

¹⁴T. E. Itina, V. N. Tokarev, W. Marine, and M. Autric, *J. Chem. Phys.* **106**, 8905 (1997).

¹⁵F. Garrelie, J. Aubreton, and A. Catherinot, *J. Appl. Phys.* **83**, 5075 (1998).

¹⁶J. C. S. Kools, *J. Appl. Phys.* **74**, 6401 (1993).

¹⁷M. Aden, E. Beyer, G. Herziger, and H. Kunze, *J. Phys. D* **25**, 57 (1992).

¹⁸M. Aden, E. W. Kreutz, and A. Voss, *J. Phys. D* **26**, 1545 (1993).

¹⁹J. R. Ho, C. P. Grigoropoulos, and J. A. C. Humphrey, *J. Appl. Phys.* **78**, 4696 (1995).

²⁰J. R. Ho, C. P. Grigoropoulos, and J. A. C. Humphrey, *J. Appl. Phys.* **79**, 7205 (1996).

²¹C. L. Liu, J. N. Leboeuf, R. F. Wood, D. B. Geobegan, J. M. Donato, K. R. Chen, and A. A. Puzetky, *Mater. Sci. Eng., B* **47**, 70 (1997).

²²R. F. Wood, K. R. Chen, J. N. Leboeuf, A. A. Puzetky, and D. B. Geobegan, *Phys. Rev. Lett.* **79**, 1571 (1997).

²³A. V. Bulgakov and N. M. Bulgakova, *J. Phys. D* **28**, 1710 (1995).

²⁴A. V. Gusarov, A. G. Gnedovets, and I. Smurov, *J. Appl. Phys.* **88**, 4352 (2000).

²⁵A. V. Gusarov and I. Smurov, *J. Phys. D* **36**, 2962 (2003).

²⁶T. E. Itina, J. Hermann, Ph. Delaporte, and M. Sentis, *Phys. Rev. E* **66**, 066406 (2002).

²⁷T. E. Itina, J. Hermann, Ph. Delaporte, and M. Sentis, *Appl. Surf. Sci.* **208–209**, 27 (2003).

- ²⁸K. R. Chen, J. N. Leboeuf, R. F. Wood, D. B. Geohegan, J. M. Donato, C. L. Liu, and A. A. Puretzky, *Appl. Surf. Sci.* **96–98**, 14 (1996).
- ²⁹L. Balazs, R. Gijbels, and A. Vertes, *Anal. Chem.* **63**, 314 (1991).
- ³⁰A. Bogaerts, Z. Y. Chen, R. Gijbels, and A. Vertes, *Spectrochim. Acta, Part B* **58**, 1867 (2003).
- ³¹H. C. Le, D. E. Zeitoun, J. D. Parisse, M. Sentis, and W. Marine, *Phys. Rev. E* **62**, 4152 (2000).
- ³²D. Bhattacharya, R. K. Singh, and P. H. Holloway, *J. Appl. Phys.* **70**, 5433 (1991).
- ³³J. H. Yoo, S. H. Jeong, R. Greif, and R. E. Russo, *J. Appl. Phys.* **88**, 1638 (2000).
- ³⁴N. M. Bulgakova and A. V. Bulgakov, *Appl. Phys. A: Mater. Sci. Process.* **73**, 199 (2001).
- ³⁵X. Mao and R. E. Russo, *Appl. Phys. A: Mater. Sci. Process.* **64**, 1 (1997).
- ³⁶D. R. Lide, *CRC Handbook of Chemistry and Physics*, 83rd ed. (CRC, Boca Raton, FL, 2002).
- ³⁷P. Atkins and J. de Paula, *Atkins' Physical Chemistry*, 7th ed. (Oxford University, Oxford, 2002).
- ³⁸R. B. Bird, W. E. Stewart, and E. N. Lightfoot, *Transport Phenomena* (Wiley, New York, 1960).
- ³⁹P. J. Shayler and M. T. C. Fang, *J. Phys. D* **10**, 1659 (1977).
- ⁴⁰L. Spitzer, *Physics of Fully Ionized Gases* (Interscience Publishers, London, 1956).
- ⁴¹J. F. Ready, *Effects of High Power Laser Radiation* (Academic, New York, 1971).
- ⁴²L. J. Rakziemski and D. A. Cremers, *Laser-Induced Plasmas and Applications* (Marcel Dekker Inc., New York, 1989).
- ⁴³L. D. Landau and E. M. Lifschitz, *Fluid Mechanics* (Pergamon, New York, 1959).
- ⁴⁴C. J. Knight, *AIAA J.* **17**, 519 (1979).
- ⁴⁵G. Callies, P. Berger, and H. Huëgel, *J. Phys. D* **28**, 794 (1995).
- ⁴⁶S. Amoruso, R. Bruzzese, N. Spinelli, and R. Velotta, *J. Phys. B* **32**, R131 (1999).